

Shizhao Wang

Assistant Professor
The State Key Laboratory of Nonlinear Mechanics,
Institute of Mechanics,
Chinese Academy of Sciences,
Beijing 100190, China
e-mail: wangsz@lnm.imech.ac.cn

Luoding Zhu

Associate Professor
Department of Mathematical Sciences,
IN University-Purdue University,
Indianapolis Indianapolis, IN 46202
e-mail: lzhu@math.iupui.edu

Xing Zhang²

Associate Professor
e-mail: zhangx@lnm.imech.ac.cn

Guowei He

Professor and Director
e-mail: hgw@lnm.imech.ac.cn

The State Key Laboratory of Nonlinear Mechanics,
Institute of Mechanics,
Chinese Academy of Sciences,
Beijing 100190, China

Flow Past Two Freely Rotatable Triangular Cylinders in Tandem Arrangement¹

In this paper we investigate the interaction of two freely rotatable triangular cylinders that are placed in tandem in a laminar flow. To study how the spacing between the two cylinders may influence the dynamic behavior of the cylinders and vortical structure of the flow, we have performed a series of numerical simulations of the two-cylinder-flow system. In all the simulations, the dimensionless moment of inertia and Reynolds number are fixed to 1.0 and 200, respectively. Four cases with the spacing ratio (L/D) of 2.0, 3.0, 4.0, and 5.0 are studied. With the increase of spacing, three different states of motion of the system are found. At $L/D = 2.0$, oscillatory rotation (swinging in both directions) is observed. At $L/D = 3.0$ both cylinders exhibit quasi-periodic autorotations. At $L/D = 4.0$ and 5.0, a more complicated pattern (irregular autorotation) is observed. For each case, the time history of angular velocity, the phase portrait (angular acceleration versus angular velocity,) and the spectra of the moments of forces on both cylinders are plotted and analyzed. The vortical structures in the near and far wake are visualized. Physical interpretations for various phenomenon observed are presented whenever possible. [DOI: 10.1115/1.4004637]

1 Introduction

The interaction of multiple bodies in a viscous flow is ubiquitous in nature and engineering applications. For example, a school of swimming fish in the ocean or a cluster of particles/droplets/bubbles moving in a fluid in chemical engineering devices. Specifically, there are three types of interactions underlying these complex phenomenon, i.e., fluid-body interaction, wake interaction, and direct-contact interaction among the bodies. Here we only focus on the first two types of interactions.

Deformable body immersed in a fluid is a typical case where fluid-body interaction occurs. To tackle this type of problem, the equations of elasticity for the bodies have to be coupled with the Navier-Stokes equations for the fluid (two-way coupling). Although such two-way coupling is not present when stationary bodies are placed in a stream or bodies undergo a prescribed motion, it does exist in cases where the rigid bodies move freely in a fluid. In such problems, the Newton's second law governing the motion of the body has to be coupled with the Navier-Stokes equations. In the present work, one of such cases is studied, i.e., two freely rotatable triangular cylinders are placed in tandem in a viscous flow.

Flow-induced rotation is an interesting phenomenon that we often observe in nature and is closely related to applications in wind engineering, aeroballistics, and meteorology. In this problem, the rotation of the body is driven by the unsteady hydrodynamic moment of force. On the other hand, the rotating body surface also acts as a time-dependent boundary condition for the surrounding flow. The study of this phenomenon can date back to as far as 1853 when Maxwell [1] first analyzed the behavior of a falling paper and categorized the motion into "fluttering" (side-to-side motion) and "tumbling" (end-over-end rotation). Since

then, researchers have attempted to develop a better understanding of this behavior by modeling and experimentation. Early experimental studies on this subject can be found in [2] and [3]. Lugt [4] first conducted numerical simulations to study the "autorotation" of an elliptic cylinder (autorotation is defined as the continuous rotation of a freely rotatable body in a flow in the absence of any other driving forces). Some works on the subject of autorotation were reviewed in [5]. Skews [6] studied the effect of thickness-to-chord ratio on the autorotation of a rectangular plate. Skews [7] studied the autorotation of many-sided bodies in an airstream by laboratory experiments and found that among the cross section of equilateral polygons the triangular prisms rotate fastest and polygons with more than eight sides do not autorotate. Skews [8] further studied the autorotation of polygonal prisms with an upstream vane. Zaki et al. [9] studied the autorotation of a square cylinder both numerically and experimentally and attempted to model the dynamics of the cylinder by a nonlinear ordinary differential equation. Copeland [10] proposed a perturbed-pendulum model for flat-plate autorotation. Mittal et al. [11] studied the effect of Reynolds number and thickness-to-length ratio on the autorotation of a plate. Srigarom and Koh [12] studied the self-excited rotational oscillation of an equilateral triangular cylinder. More studies on rotation of falling papers can be found in [13–25].

Furthermore, when multiple bodies are involved in a problem, wake interactions are present. This has attracted the attentions of many researchers because of its importance in engineering applications. Two cylinders in tandem is perhaps the most frequently studied configuration. Plenty of literatures can be found on this topic. Most of the studies focused on the interaction among stationary cylinders [26–32]. Other studies dealt with flow-induced body oscillations [33–36]. Very recently, wake interaction between two tandem flexible flags placed in a steady stream were studied experimentally in [37,38] and numerically [39].

To the best knowledge of the authors, the study of wake interaction among freely rotatable bodies is very rare in the literature. The work by our group on the two tandem rotatable cylinders in a viscous flow is probably the first such study. In this paper, we

¹Preliminary version of this paper appeared as FEDSM2009-78046 in Proceedings of ASME 2009 Fluids Engineering Division Summer Meeting, Vail, Colorado, USA, August 2–5, 2009.

²Corresponding author

Contributed by the Fluids Engineering Division of ASME for publication in the JOURNAL OF FLUIDS ENGINEERING. Manuscript received September 5, 2010; final manuscript received July 15, 2011; published online August 19, 2011. Assoc. Editor: Meng Wang.

report numerical results of flow field (especially vortex structure) together with some description and analysis of the dynamic behaviors of the two cylinders. The emphasis is placed on their dependence on the spacing of the two cylinders.

The rest of this paper is organized as follows. In Sec. 2 we outline the setup of the problem. Section 3 is a short introduction of the numerical method used in the study. The numerical observations are described Sec. 4. Finally, some conclusions are drawn in Sec. 5.

2 Problem Setup

The configuration of this problem is illustrated in Fig. 1. Two hinged equilateral triangular cylinders are placed in tandem in a uniform free stream of velocity U . In this study we assume that the flow is two-dimensional and laminar.

The governing equations for the incompressible flow can be written in a dimensionless form as

$$\frac{\partial \mathbf{u}}{\partial t} + \mathbf{u} \cdot \nabla \mathbf{u} = -\nabla p + \frac{1}{\text{Re}} \nabla^2 \mathbf{u} \quad (1)$$

$$\nabla \cdot \mathbf{u} = 0 \quad (2)$$

where u and p represent velocity vector and pressure, respectively. The Reynolds number Re is defined as

$$\text{Re} = \frac{UD}{\nu} \quad (3)$$

where D is the diameter of the circumcircle of the cylinder and ν is the kinematic viscosity of the fluid.

The dynamics of the rotating cylinders is governed by the following equation:

$$\tilde{I} \frac{d^2 \theta}{dt^2} = \tilde{C}_M \quad (4)$$

Here \tilde{I} is the dimensionless moment of inertia of the cylinder. For a triangular cylinder, \tilde{I} can be evaluated as

$$\tilde{I} = \frac{I}{\rho_f D^4 w} = \frac{\rho_s \frac{3\sqrt{3}}{256} D^4 w}{\rho_f D^4 w} = \frac{3\sqrt{3}}{256} \left(\frac{\rho_s}{\rho_f} \right) \quad (5)$$

where w is the thickness and ρ_s and ρ_f are the densities of the cylinder and the fluid, respectively.

The dimensionless moment of force \tilde{C}_M exerted on the cylinder is calculated by the surface integration

$$\tilde{C}_M = \mathbf{z} \cdot \oint_{\partial S} \left[p \mathbf{n} - \frac{1}{\text{Re}} (\nabla \mathbf{u} + \nabla^T \mathbf{u}) \cdot \mathbf{n} \right] \times \mathbf{r} ds \quad (6)$$

where \mathbf{n} is the unit norm vector on the surface of the body; \mathbf{r} is the position vector, and \mathbf{z} is the unit vector pointing out of the paper.

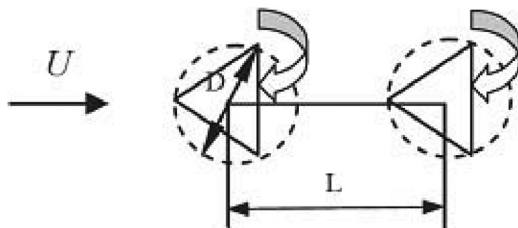


Fig. 1 A schematic diagram of the setup of the problem. Two hinged equilateral triangular cylinders are placed in tandem in a uniform free stream of velocity U . D is the diameter of the circumcircle of the triangular cylinder. L is the distance between the circumcenters of the two cylinders.

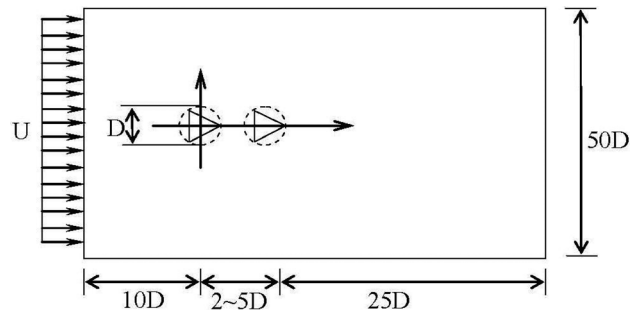


Fig. 2 The size of the computational domain. The computational domain is $37D$ – $40D$ by $50D$, with $10D$ from the inlet and $25D$ from the outlet. (The figure is not to scale.)

The relevant parameters in our problem are the Reynolds number Re , the dimensionless moment of inertia \tilde{I} , and the spacing ratio L/D .

3 Computational Method

In this study, an unstructured Chimera grid method is employed to solve the Navier-Stokes equations. This approach is very adaptable in the sense that it allows the use of multiple overlapping unstructured grids to simulate moving objects of arbitrary shapes. The solution procedure of this approach is briefly summarized here. For technical details and validations of this numerical methodology, please refer to [40]. A second-order upwind scheme is used to discretize the convective term and the Crank-Nicholson scheme is used for the temporal advancing. A SIMPLEC method is used to couple the pressure and the velocity. Different interpolation methods are designed for the velocity and the pressure on the interior boundaries to couple the solutions of different subdomains. This interpolation is incorporated into the inner loop of the velocity-pressure coupling within each time step. The equation of dynamics (4) is integrated using a leapfrog scheme [41].

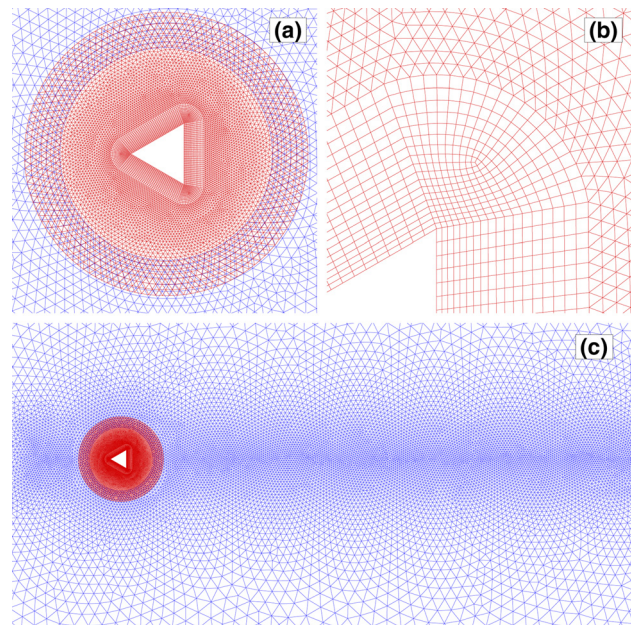


Fig. 3 Computational mesh: (a) around one cylinder, including the background mesh (in blue color) and the moving mesh (in red color); (b) zoom in near the top corner. Quadrilateral elements are deployed near the surface of the cylinder to capture the flow features in the boundary layer; (c) locally refined mesh used in the wake region (the background mesh is in blue color, and moving mesh in red color).

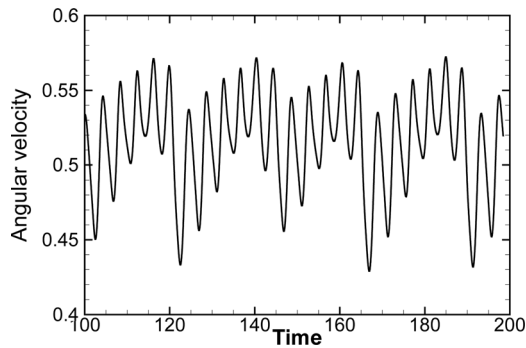


Fig. 4 Angular velocity versus time for a single cylinder. The angular velocity of the autorotation triangular cylinder is of multifrequency and quasi-periodic.

The size of the computational domain in this paper is $37D$ – $40D$ by $50D$ (see Fig. 2). The choice of this size is a compromise between the computational cost and the blocking effect from the boundaries. The total number of elements is 55,000, with 43,000 elements in the background mesh and 12,000 elements in the two submeshes that surround the two cylinders. Only triangular elements are used in the background mesh while some quadrilateral elements are deployed near the surface of the cylinder in the two submeshes to capture the flow features in the boundary layer (see Fig. 3). Each surface of the two triangular cylinders is meshed with 105 line elements. A time step of 0.005 is used in all the computations and the maximum CFL number corresponding to this time step is approximately 0.2. The grid resolution and time step in this paper are comparable to that used in [40] where reasonable results were obtained on flow over a stationary and rotating circular cylinder at the Reynolds number of 200. Mesh-independent and time step-independent tests are performed to ensure the accuracy of the solutions obtained (see Appendix A for the details).

4 Numerical Observations

There are three important dimensionless parameters in our problem: Re , \tilde{I} , and L/D . The first two parameters are fixed ($Re = 200$ and $\tilde{I} = 1.0$) while the spacing ratio varies in the range of 2.0 to 5.0. For the purpose of comparison, a simpler configuration which involves only a single triangular cylinder in a uniform flow is first investigated. The same Reynolds number and moment of inertia are also used in the single-cylinder case. The numerical observations of the flow patterns and the dynamic behaviors of the cylinders are presented as follows.

4.1 A Single Cylinder. First we perform a simulation which involves only one cylinder. Our computation begins with a *fixed* cylinder that is placed in a uniform flow. When the periodic Karman vortex street is fully developed, the cylinder is then forced to rotate impulsively with a prescribed angular velocity. After impos-

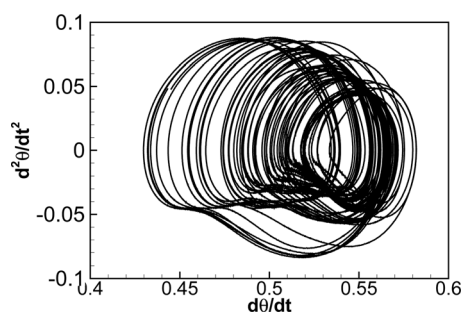


Fig. 5 Phase portrait (angular acceleration versus angular velocity) for a single cylinder. A multifrequency and quasi-periodic solution is obtained.

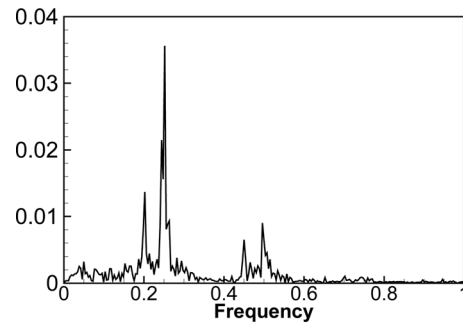


Fig. 6 Power spectrum of the moment of force on the single cylinder. Five frequencies are involved in the autorotation: 0.05, 0.20, 0.25, 0.45, and 0.50.

ing the boundary condition of constant angular velocity for some time, the cylinder is set free, i.e., its motion is now determined by the moment of force exerted on it. The direction of the initial rotation can be either anticlockwise or clockwise. Without loss of generality, we choose to start the rotation in the anticlockwise direction. It is assumed that the initial effect will disappear and an intrinsic state independent of the initial condition will be reached if the time elapsed is long enough. After this state is reached, some characteristic quantities are then recorded and analyzed. The value

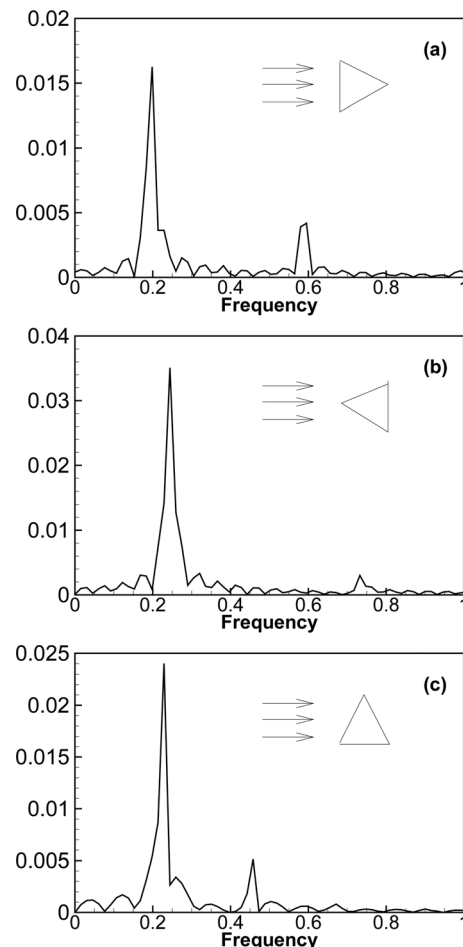


Fig. 7 Power spectrum of the moment of force on a fixed cylinder with different relative positions to the upstream flow. Three different positions are shown: (a) “back-to-flow” configuration (\triangleleft), the dominant vortex shedding frequency is 0.2; (b) “face-to-flow” configuration (\triangleright), the dominant vortex shedding frequency is 0.25; (c) “side-to-flow” configuration (\triangle), the dominant vortex shedding frequency is 0.225.

of 1.0 is used as the dimensionless initial angular velocity to start the cylinder. As that will be shown later, this value is much larger than the intrinsic terminal angular velocities (in an averaged sense) for all cases in this study. In the tandem-cylinder case, the two cylinders are also started to rotate in the same way as that in the single-cylinder case. The effects of the initial rotation on the final solution are discussed in Appendix B.

Figure 4 shows the time history of the angular velocity. It is found that a single cylinder autorotates with a dimensionless averaged angular velocity of 0.53 (which corresponds to a tip speed of $0.27U$). The pattern of fluctuation in Fig. 4 is indicative of a multi-frequency or quasi-periodic solution. This is confirmed by the

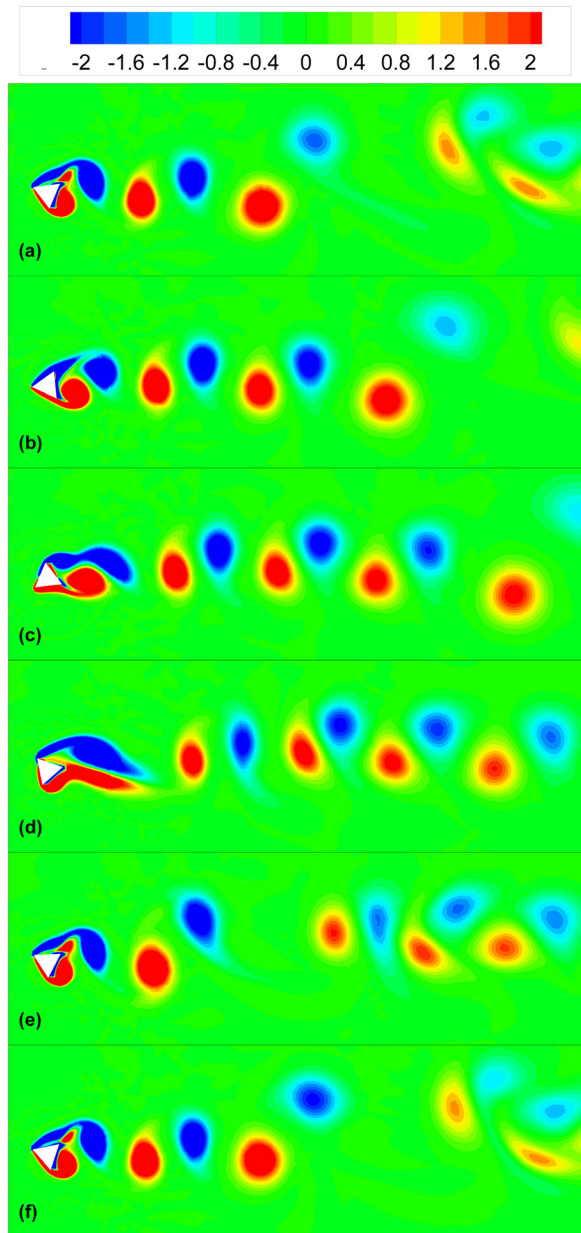


Fig. 8 Snapshots of vorticity contours during the autorotation of a single cylinder. The vortical structure resembles the regular Karman vortex street in the wake of a stationary bluff body. But, the vortex street slightly tilts up in the near wake. The distances between the vortices are not uniform because of the interaction of the autorotation and vortex shedding. (a)–(f) corresponds to $t = 155, 160, 165, 170, 175$, and 180 in Fig. 4, respectively. The slowdown of the rotation at $t = 166$ generates a gap in the contours of vorticity in (e). This gap separates the vortices into two groups.

phase portrait (angular acceleration versus angular velocity) in Fig. 5 and the power spectrum (FFT) of the moment of force in Fig. 6. The five dominant frequencies in Fig. 6 are 0.05, 0.20, 0.25, 0.45, and 0.50. The frequency of 0.25 corresponds to the averaged angular velocity of 0.53 ($(3\omega)/(2\pi)$). Some efforts are made on the origin of frequency 0.2. We first perform some simulations on a stationary cylinder at different angles to the oncoming flow and confirm that the vortex shedding frequency around a rotating triangular cylinder is most probably in the range of 0.2–0.25 (see Fig. 7). Then it is reasonable to assume that 0.2 is the asynchronous frequency of the vortex shedding and 0.25 is the “lock-in” frequency in the interaction between vortex shedding and autorotation. The frequency of 0.5 is simply a multiple of one basic frequency (2×0.25). The frequency of 0.45 is an addition of the two basic ones ($0.20 + 0.25$). The frequency of 0.05 is the difference between two basic ones ($0.25 - 0.20$).

The interaction of autorotation and vortex shedding also generates different flow structures at different phase. Six snapshots of vorticity contours are shown in Fig. 8. The vortical structure that is found in this figure resembles the regular Karman vortex street in the wake of a stationary bluff body. However, some differences do exist. First, because of the interaction between the rotating edges and the shedding vortices, the counterclockwise vortices (those in red colors) are strengthened while the clockwise vortices (those in blue colors) are weakened. As a result of this imbalance in strength, the vortex street slightly tilts up in the near wake and no longer aligns itself horizontally with the oncoming stream in the near wake. A similar oblique vortex street is observed in the flow past a rotating circular cylinder [40]. Second, vortices are not simply convected downstream. Complicated interactions such as vortex splitting, merging, and pairing/grouping can be clearly seen in the figure.

4.2 Two Tandem Cylinders at $L/D = 2.0$. The time history of the angular velocities is plotted in Fig. 9. From this figure, it is seen that instead of autorotation, both cylinders exhibit oscillatory rotation about their axes (swinging in both directions). The front and rear cylinders are found to oscillate at the same frequency but in antiphase. The amplitudes of fluctuation in angular velocity are rather small (of order 10^{-2}) for both cylinders and the amplitude of the rear one is four times larger than that of the front one. Both the phase portraits (Fig. 10) and the power spectra of moments of force (Fig. 11) indicate the existence of a period-1 solution with the frequency of 0.14. A snapshot of vorticity contours is shown in Fig. 12. It is seen from this figure that the vortex shedding behind the front cylinder is completely suppressed due to the closeness of the two. The shear layers that are generated from the two sides of the front cylinder impinge on the rear one. A vortex

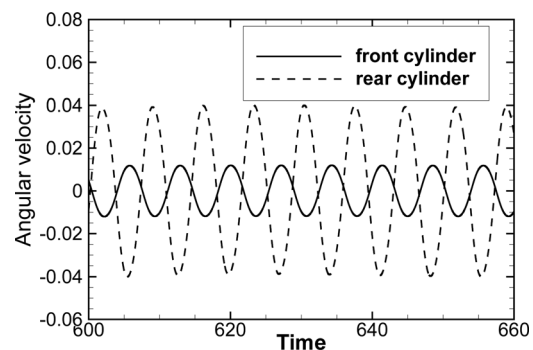


Fig. 9 Time history of the angular velocities of the two tandem cylinders in the case of $L/D = 2.0$. Solid line represents the front cylinder and dashed line represents the rear cylinder. Instead of autorotation, both cylinders exhibit oscillatory rotation about their axes. The front and rear cylinders oscillate at the same frequency but in antiphase. The amplitude of the rear one is about four times larger than that of the front one.

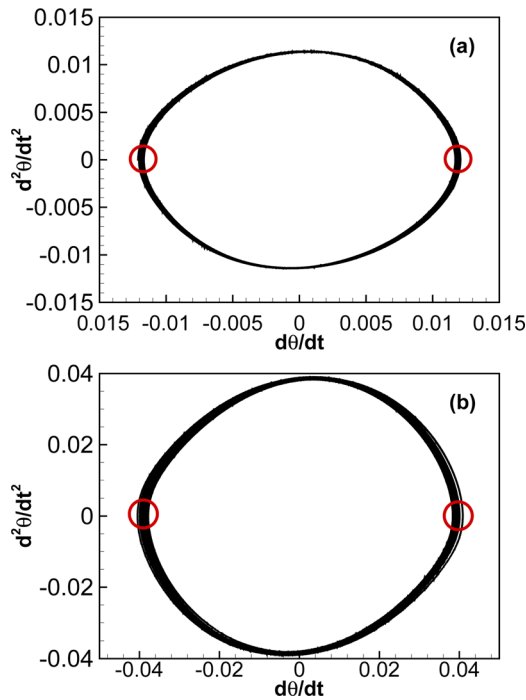


Fig. 10 Phase portraits (angular acceleration versus angular velocity) of the two tandem cylinders in the case of $L/D = 2.0$; (a) front cylinder; (b) rear cylinder. Both the oscillating of the front and rear cylinders are periodic. The open circles indicate the equilibrium positions for the point-to-point configuration.

street only exists behind the rear cylinder and no apparent vortex shedding is found in the gap. This vortex street resembles that behind a single but *elongated* bluff body (e.g., a rectangle with the dimension of $3D$ by D). In the gap between the two cylinders, the

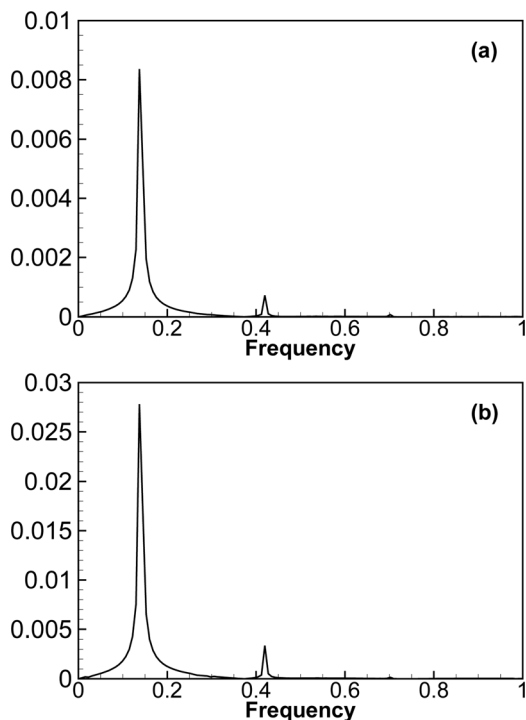


Fig. 11 Power spectra of the moments of force of the two cylinders in the case of $L/D = 2.0$; (a) front cylinder; (b) rear cylinder. The dominant oscillating frequency is 0.14 for either cylinder.

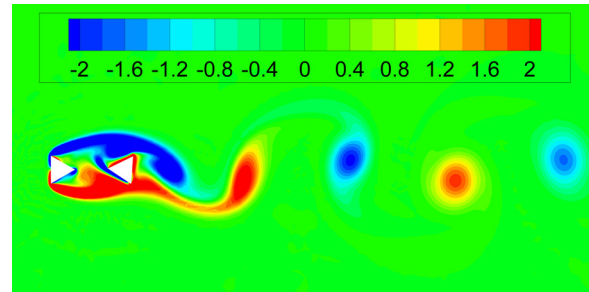


Fig. 12 The instantaneous vorticity contours for the two tandem cylinders in the case of $L/D = 2.0$. The vortex shedding behind the front cylinder is suppressed due to the closeness of the two. A vortex street only exists behind the rear cylinder.

flow is quite complicated due to the interaction of the four shear layers from the two cylinders. Presumably, both the frequency lock-in phenomenon and the threefold frequency of 0.42 (at the tiny peaks in Fig. 11) are related to the strong body-fluid-body interaction at this spacing ratio. It is interesting to point out that the point-to-point configuration ($\triangleright\triangleleft$) is the only attainable state after the memory of the initial condition is lost. The reason why the point-to-point configuration is stable but the others are not is unclear and further investigation is needed.

4.3 Two Tandem Cylinders at $L/D = 3.0$. In the case of $L/D = 3.0$, regular periodical autorotation is observed on both cylinders. The average angular velocity of the front cylinder is approximately the same as that in the single cylinder case while the rear cylinder rotates at a lower speed (see Figs. 13 and 4). Supposedly, this is caused by the fact that the velocity of oncoming flow to the rear cylinder is smaller than that to the front one in a local and average sense. Figure 14 shows the phase portraits of the two cylinders at $L/D = 3.0$. From this figure we can see that the trajectories in the phase portraits are significantly different from the case of $L/D = 2.0$. Instead of a simple loop, the trajectories are indicative of multiperiod solution which shares some similarities with those of the single cylinder case. Figure 15 shows the power spectra of the moments of force on the cylinders. In contrast with the case of $L/D = 2.0$, the spectra in the $L/D = 3.0$ case possess more peak frequencies. Compared to the single cylinder case, the spectra in this case are less noisy. The frequencies of the highest peaks are 0.24 and 0.16 for the front and rear cylinder, respectively. These two frequencies correspond to the autorotating frequencies $((3\omega)/(2\pi))$. It is observed from the simulation that

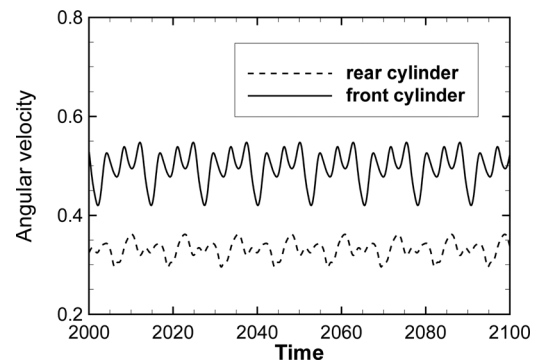


Fig. 13 Time history of the angular velocities of the two tandem cylinders in the case of $L/D = 3.0$. Solid line represents the front cylinder and dashed line represents the rear cylinder. Both the front and rear cylinders experience multiperiodic autorotation. The average angular velocity of the front cylinder is approximately the same as that of the single cylinder, and the rear cylinder rotates at a lower speed.

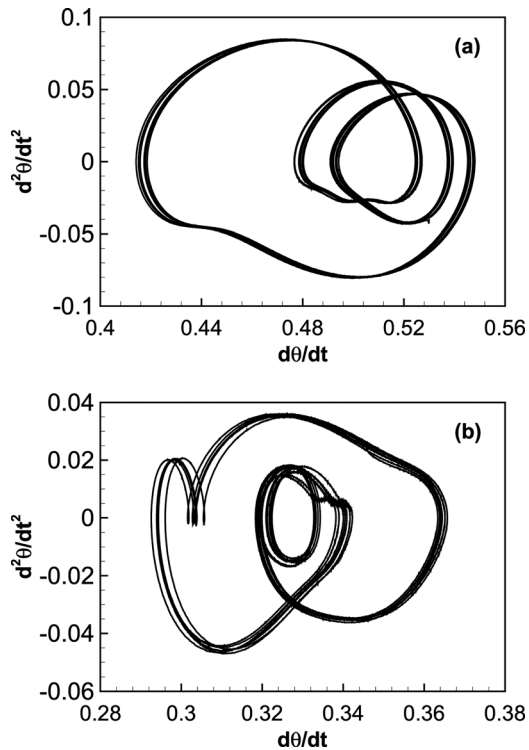


Fig. 14 Phase portraits (angular acceleration versus angular velocity) of the two tandem cylinders in the case of $L/D = 3.0$; (a) front cylinder; (b) rear cylinder. Both the autorotations of the front and rear cylinders are multiperiodic.

the vortex shedding on each cylinder is also synchronized to its own autorotation. A very interesting finding is that the frequencies of the second highest peaks are 0.16 and 0.24 for the front and rear cylinder, respectively. That is to say, the frequency of the sec-

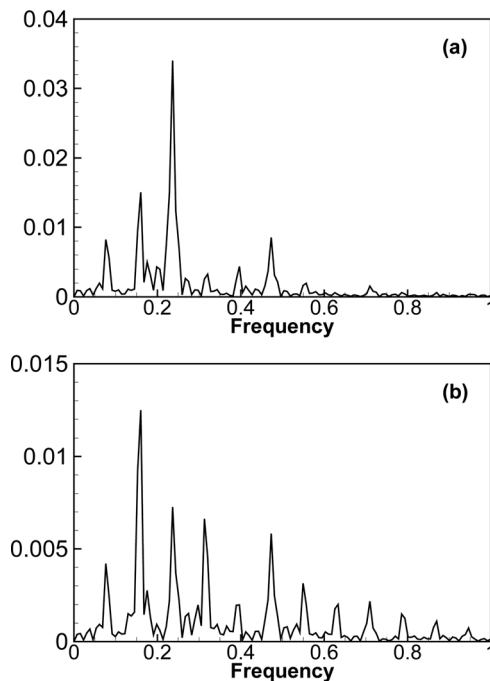


Fig. 15 Power spectra of the moments of force of the two cylinders in the case of $L/D = 3.0$; (a) front cylinder; (b) rear cylinder. Both the autorotations of the front and rear cylinder are of multifrequency. The frequencies of the highest peaks are 0.24 and 0.16 for the front and rear cylinder, respectively.

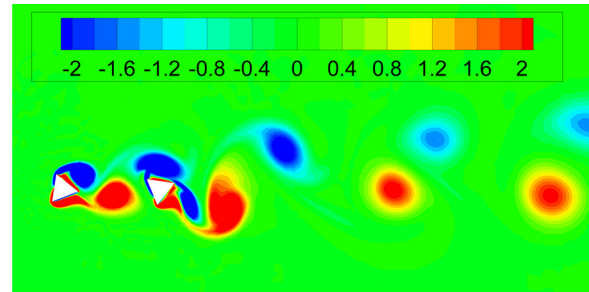


Fig. 16 The instantaneous vorticity contours for the two tandem cylinders in the case of $L/D = 3.0$. The vortex shedding from the front cylinder is fully recovered and a vortex exists in the gap between the two cylinders. A vortex street exists behind the rear cylinder.

ond highest peak on each cylinder is locked to the frequency of the highest peak on the *other* cylinder. Clearly this is a manifestation of strong interaction between the two cylinders at this spacing ratio. Another peak frequency of 0.08 can also be found on both cylinders. This frequency corresponds to the *difference* between the frequencies of the first two highest peaks (i.e., $0.24 - 0.16$). Other peak frequencies on each cylinder correspond to more complicated wake interaction. It should be pointed out that more peak frequencies of the rear cylinder are excited compared to the front one. This can be explained by the fact that more complicated

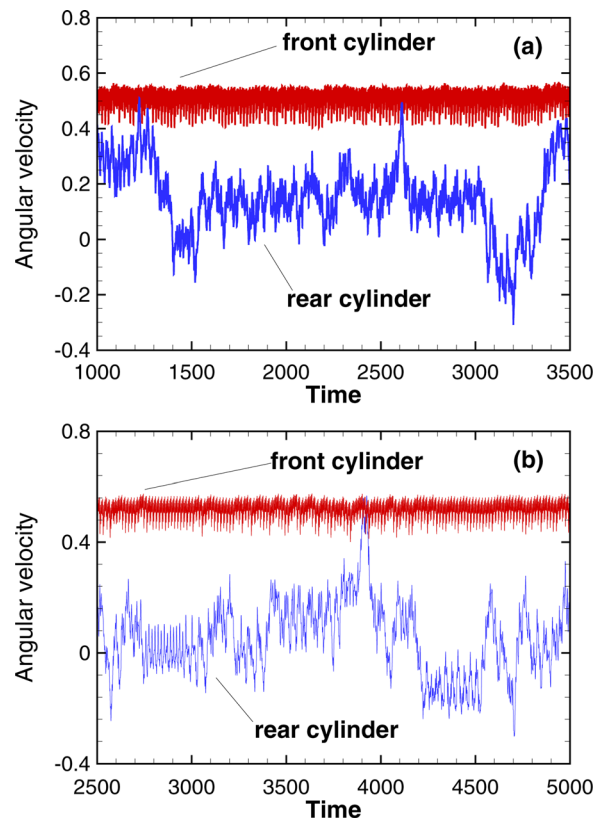


Fig. 17 Time history of the angular velocities of the two tandem cylinders at (a) $L/D = 4.0$; (b) $L/D = 5.0$. Solid line represents the front cylinder and dashed line represents the rear cylinder. The autorotations of the triangular cylinders for $L/D = 4.0$ and $L/D = 5.0$ are similar. For both cases, the triangular cylinders rotate irregularly. While the front cylinder rotates counterclockwise constantly, the rear cylinder alternates its rotating directions from time to time: it rotates counterclockwise for some time, pauses, and switches its direction and rotates clockwise for some time.

wake interaction usually occurs behind the rear cylinder. This interaction can easily affect the moment of force on the rear cylinder while its influence on the front one is relatively weaker.

A snapshot of vorticity contours is shown in Fig. 16. At this spacing ratio the vortex shedding from the front cylinder is fully recovered and a pair of alternating vortices of the opposite sign can be seen in the gap. This is consistent with the fact that the spacing between the two cylinders is approximately twice the di-

ameter D (which is roughly the size of one vortex). From the simulation it is observed that the counterclockwise vortex that sheds from the lower corner of the front cylinder will merge with a vortex of the same sign from the rear cylinder or merge with the shear layer generated on the lower corner of the rear cylinder. These two distinct patterns of merging occur *alternately* when the vortex from the front cylinder passes by the rear cylinder. This phenomenon can be explained by the fact that the shedding frequencies of two cylinders are different. The clockwise vortices at the upper corner of the front cylinder behave quite differently from those

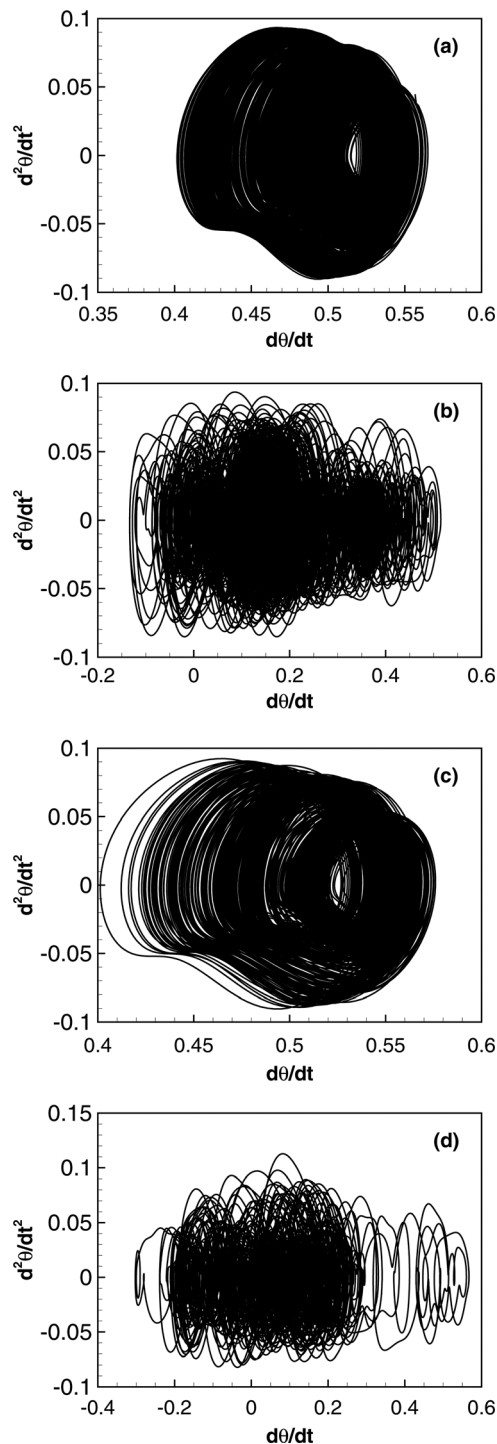


Fig. 18 Phase portraits (angular velocity versus angular velocity) of the two tandem cylinders. (a) Front cylinder, $L/D = 4.0$; (b) rear cylinder, $L/D = 4.0$; (c) front cylinder, $L/D = 5.0$; (d) rear cylinder, $L/D = 5.0$. For both cases, the autorotations of the front and rear cylinders are irregular. No periodicity can be identified on the phase portraits.

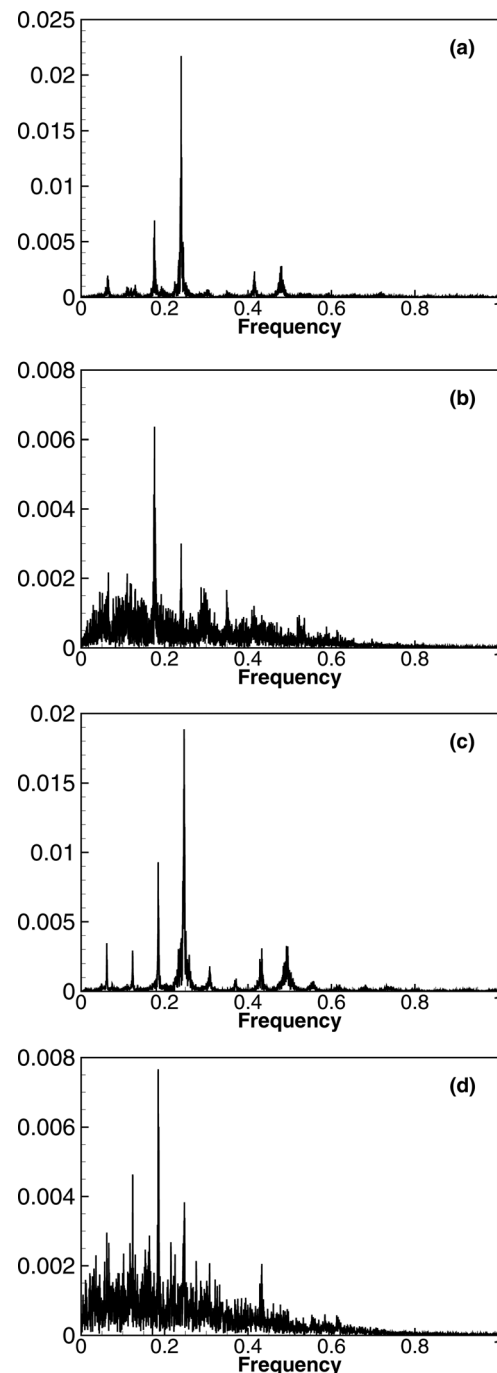


Fig. 19 Power spectra of moments of force of the two cylinders. (a) Front cylinder, $L/D = 4.0$; (b) rear cylinder, $L/D = 4.0$; (c) front cylinder, $L/D = 5.0$; (d) rear cylinder, $L/D = 5.0$. For both cases, the frequency of the highest peak is 0.25 for the front cylinder and 0.18 for the rear one. The autorotations of the rear cylinder become very noisy, and more frequencies are excited comparing with that of the front ones.

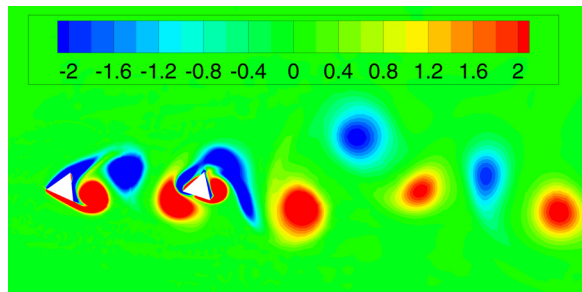


Fig. 20 The instantaneous vorticity contours for the two tandem cylinders in the case of $L/D = 4.0$. The vortex layer shedding from the front cylinder rolls up and forms a vortex street in the gap between the two cylinders. The wake structures behind the rear cylinder are irregular because of the interaction of the two cylinders.

counterclockwise ones at the lower corners. These vortices are found to impinge on the rear cylinder and are almost entirely absorbed into the shear layer of the rear cylinder. Merging of these vortices with the vortices of the same sign from the upper corner of the rear cylinder is not seen. At this spacing ratio, the vortical pattern in the far wake is also quite different from the previous case. The width of the wake is much larger because the vortices are arranged into two parallel lines rather than a single line.

4.4 Two Tandem Cylinders at $L/D = 4.0$ and $L/D = 5.0$.

When the spacing ratio is further increased to 4.0 or 5.0, a different scenario shows up. At these two spacing ratios, the flow field and vortical structure are qualitatively very similar. Thus the following descriptions may apply to both cases if not explicitly stated. At these spacing ratios, while the front cylinder rotates counterclockwise constantly, the rear cylinder alternates its rotating directions from time to time: it rotates counterclockwise for some time, pauses and switches its direction and rotates clockwise for some time. It appears that its counterclockwise spin lasts longer than the clockwise spin. It is interesting to notice that although the rear cylinder rotates in an irregular fashion, the averaged angular velocity of the front one has not changed much from that of the single cylinder case (see Figs. 17 and 4). The phase portraits and power spectra of moments of force are shown in Figs. 18 and 19, respectively. The trajectories in the phase portraits are significantly different from the previous case. The intertwining curves which appear in the phase portraits of both cylinders represent more complicated and irregular motions. From the spectra of moments of force, it is found that the frequency of the highest peak is 0.25 for the front cylinder and 0.18 for the rear one. Compared with case of $L/D = 3.0$, more peak frequencies are now excited on both cylinders, especially the rear one. The spectrum of the rear cylinder

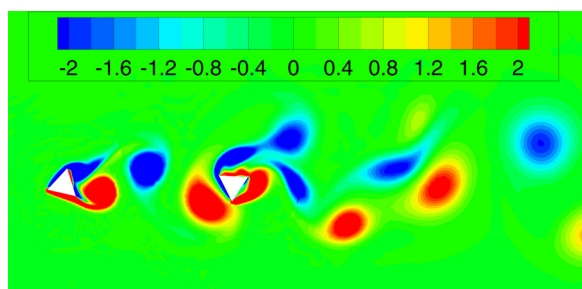


Fig. 21 The instantaneous vorticity contours for the two tandem cylinders in the case of $L/D = 5.0$. The front cylinder forms a vortex street in the gap between the two cylinders. The wake behind the rear cylinder is an interaction of the vortices shed from the two cylinders. The flow structures are similar to the $L/D = 4.0$ case.

becomes very noisy and many peaks are congested in certain range of frequency and it is very hard to identify them one by one. Presumably the complexity of the spectra is caused by the complicated vortex interactions behind the rear cylinder.

Two snapshots of vorticity contours are shown in Figs. 20 and 21, for the case of $L/D = 4.0$ and $L/D = 5.0$, respectively. It is observed from these figures that in the gap between the two cylinders, at most three (four) vortices can be found at the spacing ratio of 4.0 (5.0). At these two spacing ratios, neither the rotation nor the vortex shedding of the two cylinders is synchronized. As a result, the wake interaction pattern becomes very irregular and the vortex arrangement behind the two cylinders is quite different from all previous cases. From the simulation, very complicated

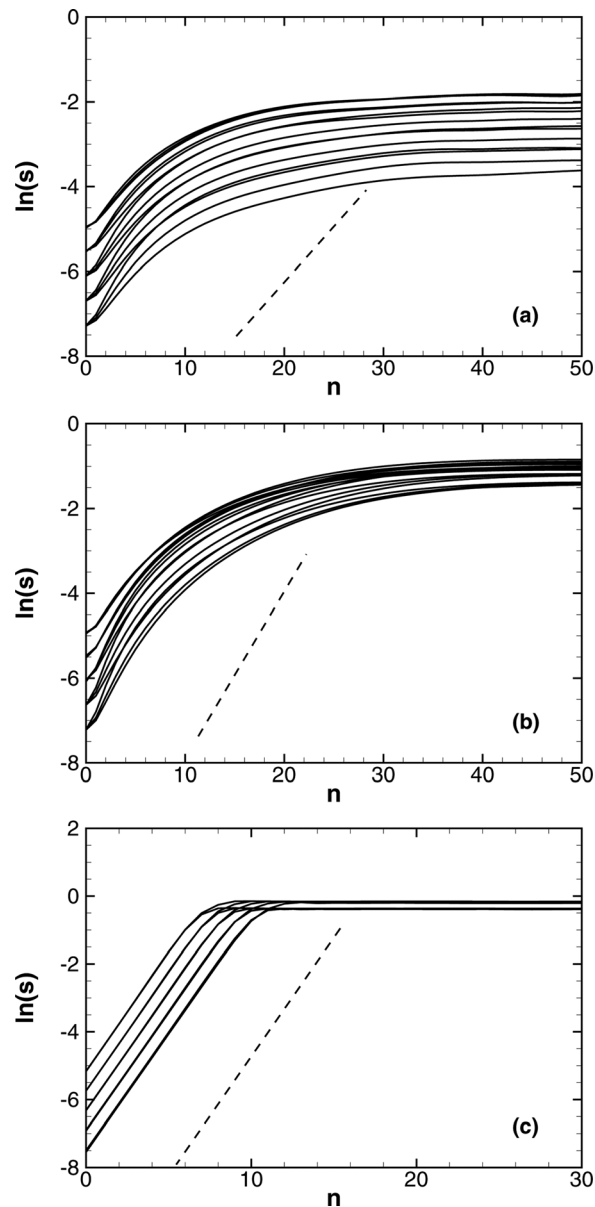


Fig. 22 The estimator as a function of the number of time steps for the data from the time series of moments of force in the case of $L/D = 5.0$: (a) front cylinder; (b) rear cylinders. [The solid lines show the results for embedding dimension $m = 4, 5$, and 6 at five different initial distances and the dashed lines are the reference lines with the slope of $\ln(1.3)$ and $\ln(1.4)$, respectively.] (c) The estimator as a function of the number of time steps for the data from the logistic map. [The solid lines show the results for embedding dimension $m = 2$ and 3 at five different initial distances. The dashed line is the reference line with the slope of $\ln(2.0)$.]

merging procedure is observed for both the clockwise and counterclockwise vortices that shed from the front cylinder.

At these two spacing ratios the time series of angular velocity, phase portraits, and power spectra all suggest that the system has become aperiodic or irregular. To rigorously verify the existence of chaos, we choose to compute the Lyapunov exponent. A positive Lyapunov exponent is indicative of an exponential divergence of nearby trajectories, i.e., chaos. The phase space reconstruction method [42–44] is used to evaluate the maximal Lyapunov exponent from the time series of moments of force on the cylinders. Consider the representation of the time series data as a trajectory in the embedding space, an estimator based on the logarithmic distance of initially nearby points on the trajectory can be computed. Figure 22 shows the estimator as a function of the number of time steps. Unfortunately, probably due to the existence of intermittency, no explicit scaling range is obtained, so that a positive Lyapunov exponent cannot be extracted. Therefore, we are not able to confirm the existence of chaos in our system. The lack of a scaling range is manifested by Fig. 22, in which the estimator computed from the data of the logistic map (a well known example of chaos) is also plotted for comparison.

5 Conclusions

We have performed a series of numerical simulations to study the interaction of two tandem rotatable triangular cylinders that are placed in a laminar viscous flow. The focus of this study is the effects of spacing ratio on the dynamic behavior and vortical structure of the two-cylinder-fluid system. With the increase of spacing ratio between the two cylinders, three different states of motion of the cylinders are found. When the two cylinders are in close proximity ($L/D = 2.0$), vortex shedding from the front one is completely suppressed. Thus only a single vortex street is formed behind the rear cylinder. As to the dynamic behavior, both cylinders exhibit low-amplitude oscillation (swinging about a $\triangleright\triangleleft$ equilibrium position). The oscillatory rotations of the two cylinders are highly synchronized. At an intermediate spacing ($L/D = 3.0$), the vortex shedding behind the front cylinder is recovered. Both cylinders exhibit multiperiod autorotation. The vortex shedding of each cylinder is synchronized to the autorotation of the other cylinder. With the increase of spacing ($L/D = 4.0$ or 5.0), the interaction between the two cylinders is weakened and more irregularity (randomness) can be seen from the dynamic behaviors (e.g., the rear one alternates its rotating direction from time to time).

There are three important dimensionless parameters which control the dynamics of the two-cylinder-fluid system: the Reynolds number Re of the flow, the dimensionless moment of inertia of the cylinders \bar{I} , and the cylinder spacing ratio L/D . In the present work, emphasis is placed on the effect of spacing ratio. It would be of interest to find out how the other two dimensionless parameters would influence the transition among these three states. However this is a very time-consuming task and we have to postpone it to the future. Furthermore, in the present study the sizes and mechanical properties of the two cylinders are exactly the same. We speculate that more dynamic modes may appear if we study the case of two cylinders with different sizes or mechanical properties. Of course, other arrangements of the two cylinders, such as side-by-side or staggered, can lead to more dynamic behaviors that are not observed here.

This two-cylinder-fluid system may also be thought of as a simple model for two adjacent solid particles moving in a viscous fluid. The findings in our paper may serve as a starting point for the understanding of the complicated interactions among rotatable particles in multiphase flows.

Acknowledgment

This work was supported by Chinese Academy of Sciences under the Innovative Projects (KJCX-SW-L08) and (KJCX3-SYW-S01); National Basic Research Program of China (973 Pro-

gram) under Project No. 2007CB814800 and National Natural Science Foundation of China under Project Nos. 10325211, 10628206, 10732090, and 10872201.

Nomenclature

\tilde{C}_M	= dimensionless moment exerted on the cylinder
D	= diameter of the circumscribed circle of the triangular cylinder
I	= moment of inertia of the cylinder
\bar{I}	= dimensionless moment of inertia of the cylinder
L	= distance between the circumcenters of the two cylinders
p	= pressure of the fluid
Re	= Reynolds number
U	= inlet flow velocity
m	= embedding dimensions in the reconstruction of phase space
w	= thickness of the cylinder
\mathbf{n}	= out-normal vector on the surface of the cylinder
\mathbf{r}	= position vector on the surface of the cylinder
\mathbf{u}	= velocity vector of the fluid
\mathbf{z}	= unit vector pointing out of the paper
ν	= kinematic viscosity of the fluid
θ	= rotating angle of the cylinder
ρ_f	= density of the fluid
ρ_s	= density of the cylinder
$\bar{\omega}$	= averaged angular velocity

Appendix A: Effects of Grid Size, Time Step Size, and Domain Size on Solution

This section describes the tests on the independence of the time step, grid size, and computational domain.

A computational domain of $37D$ – $40D$ by $50D$ is used in the simulations of two tandem cylinders (shown in Fig. 2). The computational domain for the single cylinder is $35D$ by $50D$, with $10D$ from the inlet and $25D$ from the outlet. The triangular cylinder is meshed with 105 line elements. The boundary-layer mesh with the first layer thickness of $0.01D$ and a growth factor of 1.05 is used near the surface of the cylinder (see Fig. 3). A time step of $dt = 0.005$ is used in all the computations.

A smaller time step of $dt = 0.0025$ and two larger time step of $dt = 0.01$ are also used in the simulations of a single cylinder to test the independence of the time step. The variations of angular velocity for the three cases are shown in Fig. 23. While the large time step $dt = 0.01$ causes a phase and amplitude difference, the difference between the $dt = 0.005$ case and $dt = 0.0025$ case is negligible. The time step $dt = 0.005$ is used in the present simulation.

A finer mesh and a coarser mesh are also used in the simulations of a single cylinder to test the independence of the grid size. For the finer mesh case, the surface of the triangular cylinder is

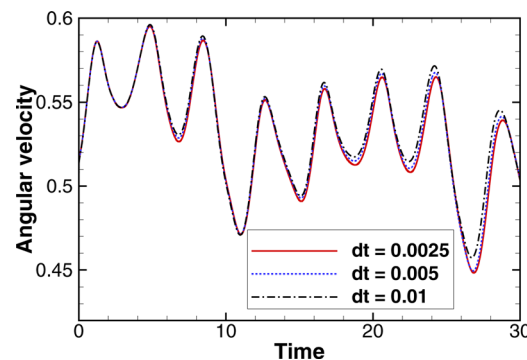


Fig. 23 The test of time step independence for an autorotating single cylinder. The large time step $dt = 0.01$ causes a phase and amplitude difference. The difference between the $dt = 0.005$ case and $dt = 0.0025$ case is negligible. The time step $dt = 0.005$ is used in the present simulations.

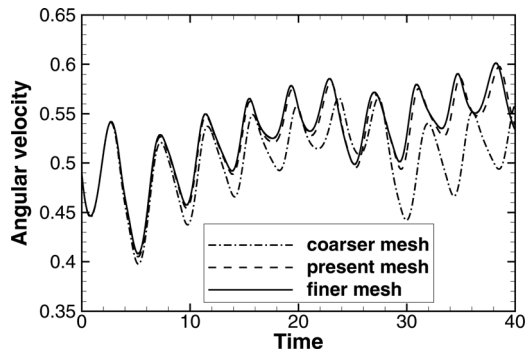


Fig. 24 The test of grid size independence for an autorotating single cylinder. For the coarse mesh, the triangle is 54 meshed with line element, the first layer thickness of the boundary-layer mesh is $0.015D$. The corresponding parameters for the present mesh are 105 and 0.01, for the fine mesh 210 and 0.05. The result on the present mesh is comparable to that on the finer mesh.

meshed with 210 line elements. The boundary-layer mesh with the first layer thickness of $0.005D$ is used. For the coarser mesh case, the surface of the triangular cylinder is meshed with 54 line elements. The boundary-layer mesh with the first layer thickness of $0.015D$ is used. The comparison of results is shown in Fig. 24. The solution based on the present grid size converges to that on the finer mesh.

A larger computational domain of $50D$ by $100D$ and a smaller computational domain of $35D$ by $30D$ are also used in the simulations of a single cylinder to test the independence of the computational domain. As shown in Fig. 25, the $35D$ by $50D$ computational domain is large enough to reduce the blocking effect.

Appendix B: Effect of Initial Angular Velocity on Solution

The effects of initial angular velocity to stir up the autorotation are discussed in this section.

A large enough impulse is needed to obtain the autorotation. Once the body picked up and stored sufficient angular momentum from the impulse to overcome the adverse torque around the stable position, the autorotation occurs and the status of the autorotation is independent of the initial impulse [5].

The computations in the present work begin with a *fixed* cylinder that is placed in a uniform flow. When the periodic Karman vortex street is fully developed, the cylinder is then forced to

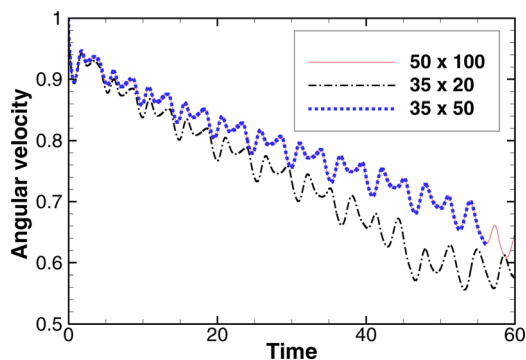


Fig. 25 The test of computational domain independence for an autorotating single cylinder. There are no difference between the result on a $50D$ by $100D$ mesh and that on a $35D$ by $50D$ mesh. The computational domain used in the present work is $35D$ by $50D$.

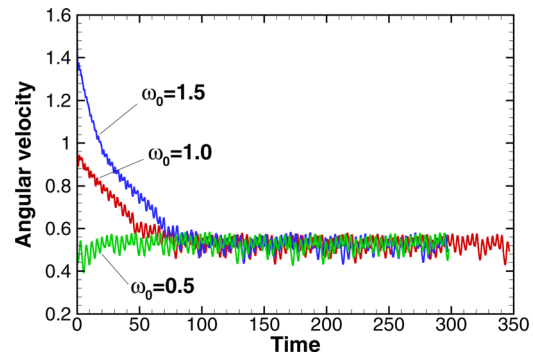


Fig. 26 The independence test of the initial angular velocity. Three different initial angular velocities are specified: $\omega_0 = 1.5$, $\omega_0 = 1.0$, and $\omega_0 = 0.5$. After the transient process the initial effect disappears and the same quasi-periodic solutions are obtained.

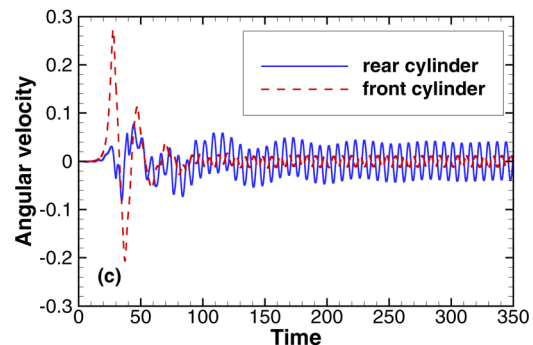
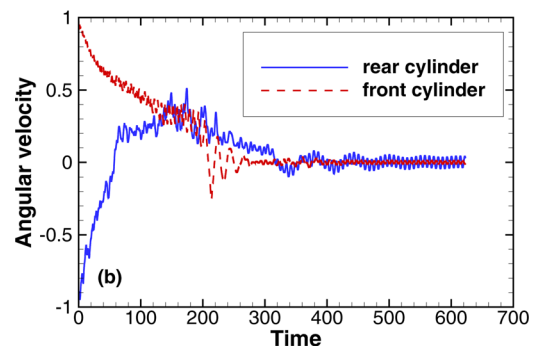
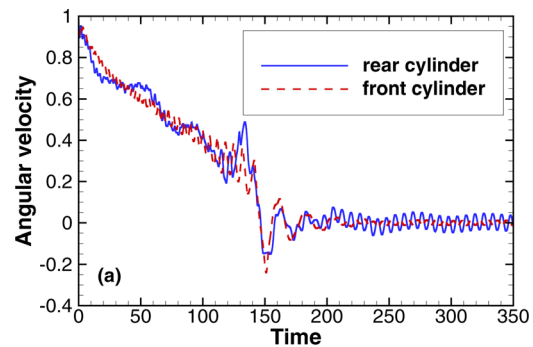


Fig. 27 The independence test of the initial angular velocity for two tandem cylinders with $L/D = 2.0$. (a) The initial angular velocities for both cylinders are counterclockwise. (b) The initial angular velocity for the front cylinder is counterclockwise, and the rear one is clockwise. (c) The initial angular velocities for both cylinders are zero. The oscillations of the two cylinders are independent of the initial angular velocities.

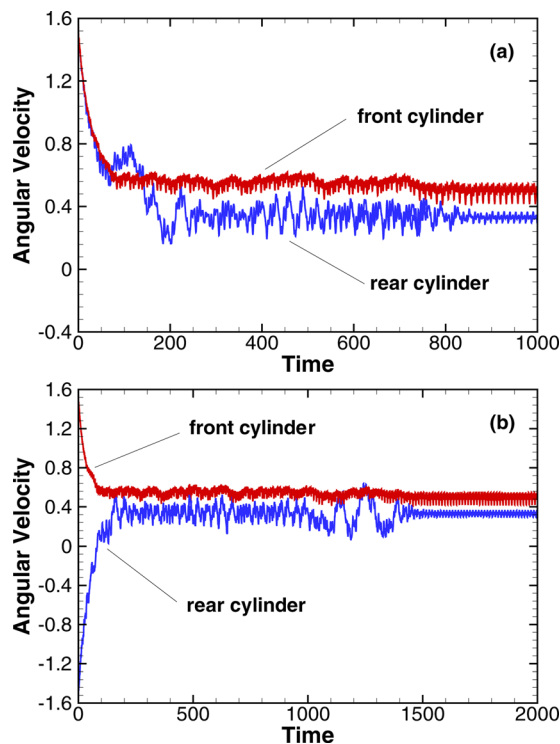


Fig. 28 The independence test of the initial angular velocity for two tandem cylinders with $L/D = 3.0$. (a) The initial angular velocities for both cylinders are counterclockwise. (b) The initial angular velocity for the front cylinder is counterclockwise, and the rear one is clockwise. The autorotations of the two cylinders are independent of the initial angular velocities.

rotate impulsively with a prescribed angular velocity. After imposing the boundary condition of constant angular velocity for some time, the cylinder is set free. The time $t = 0$ in this section is taken as the instant when the cylinder is set free.

The independence of the initial angular velocities for the autorotation of a single cylinder is shown in Fig. 26.

For the present work, the initial angular velocity $\omega_0 = 0.5$ is large enough to stir the autorotation. After the transient process, the initial effect disappears and the same quasi-periodic solutions are obtained.

Notice that only the counterclockwise initial angular velocity is prescribed and the angular velocity is also counterclockwise when the quasi-periodic solutions are obtained in the present work. Indeed, due to the symmetry of the system, when the clockwise initial angular velocity is prescribed, the final autorotation becomes clockwise.

For the two tandem cylinders, the relative initial rotating direction of the two cylinders must be considered. However, the autorotation is still independent of the initial angular velocities. As shown in Fig. 27, the same oscillating status are obtained for the tandem cylinders with $L/D = 2.0$, despite that the initial angular velocities are both counterclockwise in Fig. 27(a), and one counterclockwise and one clockwise in Fig. 27(b). Finally, because there is no autorotation in this $L/D = 2.0$ case, the zero initial angular velocities for the two cylinders also achieve the same solution [Fig. 27(c)].

As shown in Fig. 28, the autorotations for the $L/D = 3.0$ case are also independent of the initial angular velocities.

References

- [1] Maxwell, J. C., 1853, "On a Particular Case of the Descent of a Heavy Body in a Resisting Medium," *Cambridge Dublin Mathematics Journal*, **9**, pp. 115–118.

- [2] Smith, E., 1971, "Autorotating Wing: An Experimental Investigation," *J. Fluid Mech.*, **50**, pp. 513–534.
- [3] Iversen, J., 1979, "Autorotating Flat-Plate Wings: The Effect of the Moment of Inertia, Geometry and Reynolds Number," *J. Fluid Mech.*, **92**, pp. 327–348.
- [4] Lugt, H., 1980, "Autorotation of an Elliptic Cylinder About an Axis Perpendicular to the Flow," *J. Fluid Mech.*, **99**, pp. 817–840.
- [5] Lugt, H., 1983, "Autorotation," *Annu. Rev. Fluid Mech.*, **15**, pp. 123–147.
- [6] Skews, B., 1990, "Autorotation of Rectangular Plates," *J. Fluid Mech.*, **217**, pp. 33–40.
- [7] Skews, B., 1991, "Autorotation of Many-Sided Bodies in an Airstream," *Nature (London)*, **352**, pp. 512–513.
- [8] Skews, B., 1998, "Autorotation of Polygonal Prisms With an Upstream Vane," *J. Wind. Eng. Ind. Aerodyn.*, **73**, pp. 145–158.
- [9] Zaki, T., Sen, M., and el Hak, M. G., 1994, "Investigation of Flow Past a Freely Rotatable Square Cylinder," *J. Fluids Struct.*, **8**, pp. 555–582.
- [10] Copeland, C., 1994, "A Perturbed-Pendulum Model for Flat-Plate Autorotation," *J. Fluids Struct.*, **8**, pp. 125–138.
- [11] Mittal, R., Seshadri, V., and Udaykumar, H., 2004, "Flutter, Tumble and Vortex Induced Autorotation," *Theor. Comput. Fluid Dyn.*, **17**, pp. 165–170.
- [12] Srigrarom, S., and Koh, A., 2008, "Flow Field of Self-Excited Rotationally Oscillating Equilateral Triangular Cylinder," *J. Fluids Struct.*, **24**, pp. 750–755.
- [13] Willmarth, W., and Harvey, R., 1964, "Steady and Unsteady Motions and Wakes of Freely Falling Disks," *Phys. Fluids*, **7**, pp. 197–208.
- [14] Aref, H., and Jones, S., 1993, "Chaotic Motion of a Solid Through Ideal Fluid," *Phys. Fluids A*, **5**, pp. 3026–3028.
- [15] Tanabe, Y., and Kaneko, K., 1994, "Behavior of a Falling Paper," *Phys. Rev. Lett.*, **73**, pp. 1372–1375.
- [16] Mahadevan, L., Aref, H., and Jones, S., 1995, "Comment on Behavior of a Falling Paper," *Phys. Rev. Lett.*, **75**, pp. 1420–1420.
- [17] Mahadevan, L., Ryu, W., and Samuel, A., 1999, "Tumbling Cards," *Phys. Fluids*, **11**, pp. 1–3.
- [18] Field, S., Klaus, M., Moore, M., and Nori, F., 1997, "Chaotic Dynamics of Falling Disks," *Nature (London)*, **388**, pp. 252–254.
- [19] Belmonte, A., Eisenberg, H., and Moses, E., 1998, "From Flutter to Tumble: Inertial Drag and Froude Similarity in Falling Paper," *Phys. Rev. Lett.*, **81**, pp. 345–348.
- [20] Pesavento, U., and Wang, Z., 2004, "Falling Paper: Navier-Stokes Solutions, Model of Fluid Forces, and Center of Mass Elevation," *Phys. Rev. Lett.*, **93**, p. 144501.
- [21] Andersen, A., Pesavento, U., and Wang, Z., 2005, "Unsteady Aerodynamics of Fluttering and Tumbling Plates," *J. Fluid Mech.*, **541**, pp. 65–90.
- [22] Andersen, A., Pesavento, U., and Wang, Z., 2005, "Analysis of Transitions Between Fluttering, Tumbling and Steady Descent of Falling Cards," *J. Fluid Mech.*, **541**, pp. 91–104.
- [23] Jones, M., and Shelley, M., 2005, "Falling Cards," *J. Fluid Mech.*, **540**, pp. 393–425.
- [24] Bonisch, S., and Heuveline, V., 2007, "On the Numerical Simulation of the Stationary Free Fall of a Solid in a Fluid. I. The Newtonian Case," *Comput. Fluids*, **36**, pp. 1434–1445.
- [25] Jin, C., and Xu, K., 2008, "Numerical Study of the Unsteady Aerodynamics of Freely Falling Plates," *Comm. Comp. Phys.*, **3**, pp. 834–851.
- [26] Zdravkovich, M., 1977, "Review of Flow Interference Between Two Circular Cylinders in Various Arrangements," *ASME J. Fluids Eng.*, **99**, pp. 618–633.
- [27] Zdravkovich, M., 1987, "The Effects of Flow Interference Between Two Circular Cylinders in Various Arrangements," *J. Fluids Struct.*, **1**, pp. 239–261.
- [28] Mittal, S., Kumar, V., and Raghuvanshi, A., 1997, "Unsteady Incompressible Flows Past Two Cylinders in Tandem and Staggered Arrangements," *Int. J. Numer. Methods Fluids*, **25**, pp. 1315–1344.
- [29] Meneghini, J., Saltara, F., Siqueira, C., and JR, J. F., 2001, "Numerical Simulation of Flow Interference Between Two Circular Cylinders in Tandem and Side-by-Side Arrangements," *J. Fluids Struct.*, **15**, pp. 327–350.
- [30] Sharman, B., Lien, F., Davidson, L., and Norberg, C., 2005, "Numerical Predictions of Low Reynolds Number Flows Over Two Tandem Circular Cylinders," *Int. J. Numer. Methods Fluids*, **47**, pp. 423–447.
- [31] Zhou, Y., and Yiu, M., 2006, "Flow Structure, Momentum and Heat Transport in a Two-Tandem-Cylinder Wake," *J. Fluid Mech.*, **548**, pp. 17–48.
- [32] Alam, M., and Zhou, Y., 2008, "Strouhal Numbers, Forces and Flow Structures Around Two Tandem Cylinders of Different Diameters," *J. Fluids Struct.*, **24**, pp. 505–526.
- [33] Papaioannou, G., Yue, D., Triantafyllou, M., and Karniadakis, G., 2006, "Evidence of Holes in the Arnold Tongues of Flow Past Two Oscillating Cylinders," *Phys. Rev. Lett.*, **96**, p. 014501.
- [34] Deng, J., Shao, X., and Yu, Z., 2007, "Hydrodynamics Studies on Two Traveling Wavy Foils in Tandem Arrangement," *Phys. Fluids*, **19**, p. 113104.
- [35] Papaioannou, G., Yue, D., Triantafyllou, M., and Karniadakis, G., 2008, "On the Effect of Spacing on the Vortex-Induced Vibrations of Tandem Cylinders," *J. Fluids Struct.*, **24**, pp. 833–854.
- [36] Kim, S., Alam, M., Sakamoto, H., and Zhou, Y., 2009, "Flow-Induced Vibrations of Two Circular Cylinders in Tandem Arrangement. Part I: Characteristics of Vibration," *J. Wind. Eng. Ind. Aerodyn.*, **97**, pp. 304–311.
- [37] Ristroph, L. and Zhang, J., 2008, "Anomalous Hydrodynamic Drafting of Interacting Flapping Flags," *Phys. Rev. Lett.*, **100**, p. 228104.
- [38] Jia, L., and Yin, X., 2008, "Passive Oscillations of Two Tandem Flexible Filaments in a Flowing Soap Film," *Phys. Rev. Lett.*, **101**, p. 194502.

- [39] Zhu, L., 2009, "Interaction of Two Tandem Deformable Bodies in a Viscous Incompressible Flow," *J. Fluid Mech.*, **635**, pp. 455–475.
- [40] Zhang, X., Ni, S., and He, G., 2008, "A Pressure-Correction Method and Its Applications on an Unstructured Chimera Grid," *Comput. Fluids*, **37**, pp. 993–1010.
- [41] Morton, K., and Mayers, D., 1994, *Numerical Solution of Partial Differential Equations: An Introduction*, Cambridge University Press, Cambridge.
- [42] Cao, L., Hong, Y., Zhao, H., and He, G., 1995, "Predicting Chaotic Time Series With Wavelet Networks," *Physica D*, **85**, pp. 225–238.
- [43] Kantz, H., and Schreiber, T., 1997, *Nonlinear Time Series Analysis*, Cambridge University Press, Cambridge.
- [44] Hegger, R., Kantz, H., and Schreiber, T., 1999, "Practical Implementation of Nonlinear Time Series Methods: The Tisean Package," *Chaos*, **9**, pp. 413–435.